J Therm Spray Tech (2023) 32:234–248
https://doi.org/10.1007/s11666-022-01475-0

PEER REVIEWED

Properties of Multilayered Metallic Coatings Deposited on Carbon Fiber-Reinforced Polymers (CFRPs) through Electrochemical and Cold Spray Processes

Panteha Fallah[1] · Sima A. Alidokht[1,2] · Phuong Vo[3] · Richard R. Chromik[1] · André McDonald[4] · Stephen Yue[1]

Submitted: 12 July 2022 / in revised form: 17 September 2022 / Accepted: 28 September 2022 / Published online: 18 October 2022
© Crown 2022 2022

Abstract Previous studies have shown that copper (Cu) may be cold spray deposited on epoxy carbon fiber-reinforced polymers (CFRPs) if an interlayer Cu of electroplated on an electroless nickel (Ni) coating is present prior to cold spraying. In this present study, the tensile adhesion bond strength of these multilayered metallic coatings was measured in accordance with ASTM Standard C-633-13. Fractured surfaces after tensile adhesion testing were examined by scanning electron microscopy (SEM) and optical microscopy (OM). Scratch adhesion testing from the polished cross sections of the multilayered coatings was also performed to compare the results with those obtained from the tensile adhesion testing. The microstructure of the cold-sprayed and electroplated Cu coatings was analyzed by electron channeling contrast imaging (ECCI), and its correlation with hardness values was studied. Adhesive failure at the Ni coating/CFRP interface was observed in the absence of a cold-sprayed Cu coating. Enhanced bonding between electroless Ni coating and exposed carbon fiber areas was observed relative to the epoxy regions. This enhanced bonding was attributed to the increased roughness of the carbon fiber regions relative to the epoxy areas. However, after cold spraying with Cu, cohesive failure of the cold-sprayed Cu coating occurred, which was likely due to insufficient plastic deformation of the particles cold sprayed close to the critical velocity of Cu. Electron channeling contrast imaging analysis from the cross sections revealed uniform and inhomogeneous microstructures within the electroplated and cold-sprayed Cu coatings, respectively.

Keywords adhesive failure · cohesive failure · grain size · microstructure · scratch adhesion testing · tensile adhesion bond strength

✉ Panteha Fallah
Panteha.fallah@mail.mcgill.ca

[1] Department of Mining and Materials Engineering, McGill University, Montreal, QC H3A 0C5, Canada

[2] Department of Mechanical and Mechatronics Engineering, Faculty of Engineering and Applied Science, Memorial University of Newfoundland, St. John's, NL A1B 3X5, Canada

[3] National Research Council Canada, Boucherville, QC, Canada

[4] Department of Mechanical Engineering, University of Alberta, Edmonton, AB T6G 1H9, Canada

Introduction

Metallization of polymeric substrates such as carbon fiber-reinforced polymers (CFRPs) has gained significant interest in the aerospace industry over the past few decades. Carbon fiber-reinforced polymers are advantageous due to their high specific strength; however, they are more electrically resistive than aluminum, limiting their applications (Ref 1). Different coating methods are available for metalizing polymers, including physical vapor deposition (PVD) and chemical vapor deposition (CVD), but, with these techniques, only very thin films (below 100 μm) can be deposited on the substrates (Ref 2-4). High-temperature thermal spray technologies, including wire arc spray, flame spray and air plasma spray, can be used to achieve thick coatings. However, thermal degradation of the polymeric structures and oxidation of metallic powders may take place during thermal spray processes (Ref 5-8).

Cold spraying uses relatively lower temperatures (below the melting point of the sprayed material) as compared to

other thermal spray techniques (Ref 9). As a result, oxidation of metallic powders, accumulation of tensile residual stress and damage to the heat-sensitive materials, such as polymeric substrates, are minimized (Ref 10). In this solid-state deposition process, particles are accelerated to a high velocity (ranging from 500 to 1200 m/s) through a converging–diverging nozzle onto a substrate to form a dense metallic coating (Ref 11).

In cold spraying metallic powders onto metallic substrates, bonding between the particles and the substrate occurs through metallurgical bonding and/or mechanical interlocking (Ref 12). However, cold spraying metallic powders onto polymeric substrates and polymer-based composites are challenging due to their poor erosion resistance, limiting coating formation and growth on these substrates (Ref 13). Thermoplastic substrates are more amenable to cold spraying as they have better ductility than brittle thermosets, allowing for particle embedding (mechanical interlocking) as opposed to the brittle fracture and erosion of the thermosetting substrates (Ref 14). Thus, bonding between metallic powders and the polymeric substrate is achieved by mechanical interlocking.

Polymeric substrates and polymer-based composites have been successfully cold sprayed with a variety of metallic powders such as tin (Sn) (Ref 13), iron (Ref 15), aluminum (Ref 16), copper (Ref 17) and 316L stainless steel (Ref 18). However, these coatings showed some issues related to the delamination/insufficient coating adhesion (Ref 17), low deposition efficiency (DE) and substrate damage and erosion that have limited further coating growth (Ref 19). In previous studies (Ref 14, 20-22), the adhesion/cohesion properties of the cold-sprayed coatings deposited on a polymeric substrate were found to be relatively low (below 30 MPa) when compared with a coating cold sprayed on metallic substrates. It was reported that soft metallic powders such as Sn can be cold sprayed on thermosetting epoxy-CFRP through the "crack filling" mechanism. It was hypothesized that partially melted or thermally softened particles impact the substrate, and the solid core of the particle generates microcracks which were subsequently filled by the molten part of the Sn particle, allowing for mechanical interlocking (Ref 13). However, Che et al. (Ref 13) and Liberati et al. (Ref 23, 24) reported low adhesion/cohesion bond strength of tin (Sn) and Sn mixed with different secondary metallic powders cold sprayed onto a variety of CFRP substrates with different surface finishes (bond strength was varied from 2 to 20 MPa). They observed the full range of failure types (adhesive, cohesive and a mixture of adhesive-cohesive) depending on the sprayed material, spray condition and the CFRP surface characteristics. Ganesan et al. (Ref 21) obtained shear adhesion strengths below 3 MPa when cold spraying Cu onto a polyvinyl chloride (PVC) substrate. Małachowska et al. (Ref 25) achieved an adhesion strength of only 3.6 MPa for cold-sprayed Cu coating deposited onto polyamide 6 substrates at a gas pressure of 0.9 MPa. Rezzoug et al. (Ref 26) modified the CFRP surface with various interlayers (aluminum mesh layer) and fillers (pure copper and a mixture of copper and stainless steel powders) before spraying zinc via the wire-arc spray technique. They found that surface modification greatly affected adhesion bonding between the coating and the modified substrate. In the case of pure Cu filler, adhesion strength was not improved due to the smooth topography of the substrate after applying the Cu powder filler which was measured to be 2.7 MPa. Stainless steel powders mixed with Cu powder led to the generation of a rougher surface finish as compared to that of pure Cu powder filler due to the irregular morphology of stainless steel powder. As a result, mechanical interlocking was enhanced, and adhesion strength was 5.1 MPa. In the case of the aluminum mesh layer, the highest adhesion was achieved and found to be 6.5 MPa.

There are two distinct deposition steps when cold spraying onto polymeric substrates: (1) first-layer deposition that occurs between the impinged metallic particles and the polymeric substrate and (2) build-up that occurs between the metallic powders and the previously deposited particles (Ref 15). Coating thickness growth is challenging in each deposition step due to the completely different properties of the substrates (polymeric surface versus the first layer of metallic coating). Barletta et al. (Ref 19) successfully cold-sprayed Cu onto a thermoplastic (PA66) substrate for various cold spray exposure times. They found rapid coating growth initially (from 0 to 6 s) through the embedding of the Cu particles into the polymeric substrate. However, coating deposition slowed down after fabrication of the very first metallic layer, because Cu particles impacted on a much harder substrate (Cu coating) as compared to the soft polymeric substrate, preventing further coating growth.

Fabrication of metallic interlayers onto an epoxy-CFRP substrate prior to cold spraying Cu was proposed recently to avoid substrate damage, increase DE and enhance bonding formation (Ref 27). The presence of a Cu interlayer with an almost similar hardness as the Cu powder permitted mutual plastic deformation of both material couples, likely allowing for successful cold spray deposition (Ref 28). This study aims to evaluate and understand the adhesion/cohesion properties and microstructure of the multilayered metallic coatings fabricated in a previous study (Ref 27) onto a CFRP substrate through tensile and scratch adhesion testing, and electron channeling contrast imaging (ECCI), respectively. The CFRP substrate was first metallized with an electroless Ni (EN) coating to enable the fabrication of a subsequent interlayer through

electroplating of a 100 μm Cu coating followed by cold spraying Cu at various gas pressures of 60-68 psi. Top and cross-sectional SEM images of the cold-sprayed Cu coatings have been presented elsewhere (Ref 27). The configuration of multilayered metallic coatings is abbreviated as EN-Cu_1-Cu_2, where EN refers to the electroless Ni coating, Cu_1 is the electroplated Cu coating, and Cu_2 is the cold-sprayed Cu coating.

Experimental Methodology

Materials, Metallization Steps and Conditions

Oxygen-free Cu powder (PG-PMP-1012, Plasma Giken Co., Ltd., Saitama, Japan) was used as the feedstock powder. Its characteristics were examined previously (Ref 27) and are summarized in Table 1. The particle size of the Cu powder was assessed using a laser scattering particle size analyzer (LA-920, Horiba, Japan), and the distribution has been presented elsewhere (Ref 27). A scanning electron microscope (SU 3500, Hitachi, Japan) was used to obtain images of the Cu powder particles from the top and cross-section views (see Fig. 1). The Cu powder was nearly spherical, and its average particle size (D_{50}) was 18.9 μm, where 50% of the particles were smaller than 18.9 μm.

The substrate materials used in this study were epoxy-CFRPs, fabricated by Bombardier Aerospace (Montreal, Canada), consisting of a thermosetting epoxy matrix with continuous carbon fiber reinforcements. The CFRP panels were made of four plies of 5276-1/G30-500 epoxy carbon prepreg ([0/90]2 s). The CFRP substrates were 1.7 × 1.7 cm^2 with a thickness of 1.7 mm and were degreased with methanol prior to coating.

CFRP substrates were first activated by palladium (Pd) particles to accelerate the chemical reactions occurring in the subsequent EN deposition. A Ni-coated CFRP with 5 μm coating thickness was then electrodeposited with Cu to achieve a 100 μm Cu coating. The metallization process has been extensively described in a previous study (Ref 27).

Cold spray of Cu at low pressure was conducted with a commercially available cold spray system (KM CDS 2.2, Inovati, Santa Barbara, CA, USA). The cold spray process parameters for Cu-coated CFRP substrates are listed in Table 2. Only one pass was sprayed at each gas pressure, which ranged from 60 to 68 psi. A step size of 1 mm (20 steps) was selected, and the feeding rate was measured to be 11.5 ± 2 g/min for three measurements. The cold spray parameters were chosen based on the previously successful cold spay experiments with Cu-on-Cu interlayer (Ref 27, 28).

Single pass cold spray experiments were conducted three times for each gas pressure (n = 3), and the corresponding standard deviations were reported to be relatively small (i.e., approximately 1%) (Ref 27).

Coating Properties and Characterization

The coating adhesion/cohesion bond strength was evaluated by means of a tensile adhesion (i.e., "pull-off") test performed on coated CFRP samples after each metallization step, according to ASTM standard C-633-13 (Ref 29, 30). The modified testing required sectioning (Delta Abrasimet, Buehler, Illinois, USA) of the CFRP samples into square specimens of 1.7 × 1.7 cm^2. In this modified testing standard, the square specimens covered most of the circular surface area, thus leading to a nominal stress distribution difference with that of the circular test. A similar modification to ASTM standard C-633-13 has been made by other researchers for various cold-sprayed coatings on CFRP substrates (Ref 13, 22, 23). Although the ASTM standard C-633-13 is applicable for coatings with thickness greater than 380 μm, thin layers of "dense" coating can be tested satisfactorily. Observations from the cross-sections of all the coatings suggested the formation of dense and uniform coatings (Ref 27). Therefore, this adhesion method has been used for testing thin coatings in this study.

The coating surfaces were then ground using #2000 grit SiC polishing papers to remove any loose particles that remained from the cold spray process. A room temperature curing epoxy adhesive (J-B weld original cold weld, USA) was used to bond the coated specimens between two steel cubic blocks of 1.7 × 1.7 cm^2 with a height of 1 cm, which was machined on a 2.54 cm diameter cylindrical steel blocks (see Fig. 2). A 'room temperature' curing adhesive was selected to avoid the occurrence of any possible thermal degradation to the heat-sensitive epoxy-CFRP substrate. The modified design of the counter blocks allowed for more accurate measurements as falling glue from the sample sides can be controlled. When the epoxy adhesive was completely cured, the coating was pulled off using an MTS servo-hydraulic pressure machine at a constant crosshead speed of 1.0 mm/min. The strength of the adhesive that is the strength at which the adhesive fails was measured by performing an adhesion strength test on the

Table 1 Properties of the feedstock Cu powder

Powder	Morphology	Supplier	D_{50}, μm	Microhardness, $HV_{0.01}$
Cu	Nearly spherical	Plasma Giken	18.9	65 ± 8 (n = 7)

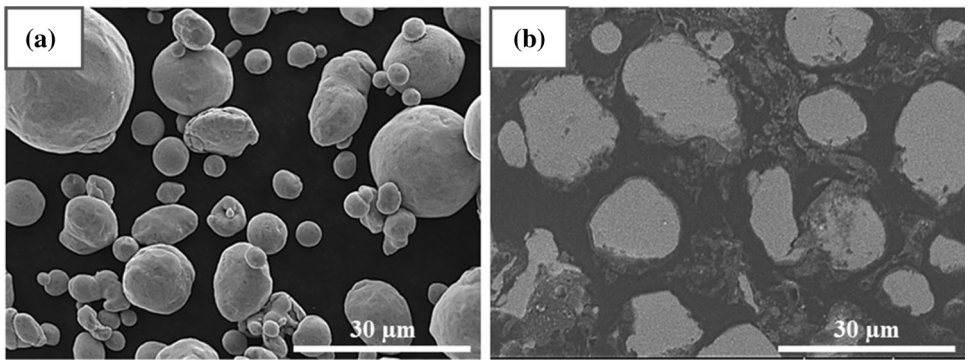

Fig. 1 SEM images of the feedstock Cu powder from (a) top and (b) polished cross-sectional views

Table 2 Cu cold spray parameters for Cu coated CFRP substrates

Powder	Carrier gas	Gas temperature, °C	Gas pressure, psi (MPa)	Stand-off distance, mm	Nozzle travel speed, mm/s
Cu	N_2	482	60 (0.41), 65 (0.45), 68 (0.46)	35	25

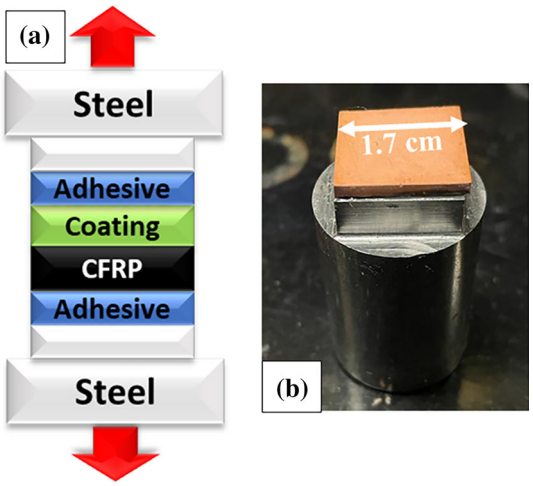

Fig. 2 (a) Adhesion strength testing setup and (b) machined steel block

two steel blocks joined with the cured glue. The fractured surfaces were then characterized with a digital microscope (VHX-5000, Keyence, Japan) and an SEM. For each coating condition, three measurements were performed, and the average strength was reported.

Scratch adhesion testing was performed according to ISO 27307 (Ref 31) to qualitatively characterize the bond strength of the multilayered metallic coatings using a scratch tester (Micro-Combi, Anton Paar, Switzerland). In this test, a Rockwell diamond stylus was drawn across the polished cross section of the coatings, starting in the substrate and ending in the cured resin. The applied normal load, speed and scratch length were 0.2 N, 3.5 mm/min and 0.5 mm, respectively. The scratch parameters were chosen based on the previously scratch testing for Cu coating (Ref 32). Scratches were then examined by SEM to identify the failure mechanism and possible inter-splat decohesion. A qualitative–quantitative comparison was then made from both tensile and scratch adhesion testing.

A cold field emission SEM (SU 8230, Hitachi, Japan) with a photodiode backscattered electron (BSE) detector was used to analyze the CFRP surface after Pd activation to obtain a correlation between the distribution of the dispersed Pd nanoparticles onto a CFRP substrate, CFRP surface topology and adhesion behavior of the EN coating to the CFRP. Compositional analysis of the CFRP after Pd activation was conducted using Energy-Dispersive x-ray Spectroscopy (EDS) in the SEM. A 3D optical surface profiler (ZYGO, Connecticut, USA) was used to determine the surface roughness and topology of the CFRP substrate before activation treatment to study the effect of CFRP surface topography on the dispersion behavior of the Pd particles over the entire CFRP surface.

Microstructural observations were performed on the polished cross-sections of the coatings to reveal the grains and deformed structures of the coatings. Cross sections of the coatings were cold mounted, mechanically grounded and polished using 9, 3 and 1 µm diamond pastes followed by 0.05 µm colloidal silica.

The morphology and microstructure of the initial Cu powder deposited and cold-sprayed Cu coatings were revealed by Electron Channeling Contrast Imaging (ECCI) using a cold field emission SEM (SU 8230, Hitachi, Japan) with a photodiode backscattered electron (BSE) detector. The accelerating voltage was in the range of 5-10 keV, and the working distance varied from 8 to 10 mm. A

correlation between the microstructure and the measured hardness of the coatings was then explored. An image analysis software (ImageJ) was used to measure the grain and particle sizes.

Results

Tensile Adhesion/Cohesion Bond Strengths

The adhesion strength results of the deposited coatings after each metallization step are shown in Fig. 3. Electroless Ni coating, electroplated and cold-sprayed Cu coatings fabricated on CFRP substrate are abbreviated as EN, Cu_1 and Cu_2, respectively. From the cross-sectional SEM images of the multilayered coatings (Ref 27), the thickness of the cold-sprayed Cu coatings increased from approximately 90 to 145 µm by increasing the gas pressure from 60 to 68 psi (Ref 27). The glue adhesion strength was determined to be 13 MPa.

In the adhesion strength test, the EN and EN-Cu_1 coatings failed at the EN/CFRP interface, indicating adhesive failure. No significant change in the adhesion bond strength of the EN and EN-Cu_1 coatings to the CFRP substrate was observed, and their adhesion bond strengths were measured to be 6.85 and 6.38 MPa, respectively. The almost similar bond strengths were possibly due to the electroplating being performed at low 'intensity' process conditions of room temperature and a very low applied current.

After cold spraying Cu on the EN-Cu_1 layer, the adhesion strength test led to the failure of the cold-sprayed Cu coatings, indicating cohesive failure. The cohesion bond strength of the cold-sprayed Cu coatings slightly increased from 1.45 to 2.45 MPa by increasing the gas pressure from 60 to 68 psi.

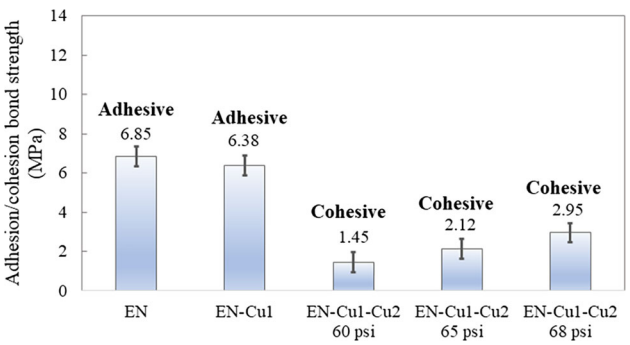

Fig. 3 Adhesion/cohesion bond strength of the coatings obtained after electroless Ni deposition (EN), Cu electrodeposition (EN-Cu_1) and Cu cold spraying (EN-Cu_1-Cu_2) at three different gas pressures of 60, 65 and 68 psi

Characterization of Fractured Surfaces in the EN and EN-Cu_1 Coating Configurations

Figure 4(a) and (b) shows the OM images of the fractured surfaces in the EN and EN-Cu_1 coating systems where adhesive failure at the EN/CFRP interface occurred. Figure 4(a) shows that damage to the epoxy took place in areas where the carbon fibers were exposed and a degree of roughening in these areas is noticeable. Figure 4(b) shows the corresponding surface of the peeled EN coating, revealing the pattern of the underlying carbon fiber region.

Figure 5(a) and (b) shows the top and cross-section views of the as-received CFRP, respectively. Figure 5(a) shows that carbon fibers (shown by white arrows) are separated by epoxy regions (shown by yellow arrows) and from the cross-sectional OM image (Fig. 5b), areas rich in carbon fibers close to the top surface and others rich in epoxy polymer can be observed.

Further SEM characterization of the carbon fiber areas was conducted after performing the adhesion test, and the corresponding SEM images of the fracture surfaces are shown in Fig. 5(c), (d), (e), (f) and (g). In Fig. 5(c), damaged epoxy in the carbon fiber regions was observed (shown by white arrows), leading to more visible exposed carbon fibers (shown by black arrows). A degree of discontinuity along the carbon fiber (i.e., broken carbon fiber) was also noticed, which is shown by the yellow arrows. Figure 5(d) and (e) shows the EDS map of the same area and the corresponding EDS results, respectively, confirming the presence of 96.1 wt.% carbon and 2.6 wt.% nickel. According to the EDS results, the bright spots in Fig. 5(c) are possibly the traces of the residual nickel, which is mostly observed in the grooves between the carbon fibers. Figure 5(f) shows the backside of the peeled EN coating which is complementary and corresponds to the pattern of the carbon fiber regions in Fig. 5(c). As shown in Fig. 5(f), linear smooth structures are the traces of the carbon fibers, and the rough area is the damaged EN coating. This result could suggest that EN coating has been mechanically interlocked in the grooves between carbon fibers where epoxy is present.

Figure 5(g) shows the polished cross-section of the EN-Cu_1 coating deposited on the carbon fiber area of the CFRP substrate. Carbon fiber regions consisted of exposed carbon fibers and epoxy polymer between them. As shown, the EN-Cu_1 coating followed the surface profile of the CFRP substrate. A unique characteristic of the electroless deposition is that a uniform coating that follows the substrate surface topography can be achieved (Ref 33-38). Possible mechanisms affecting the adhesion properties of the EN coating to the epoxy-CFRP are explained in the following section.

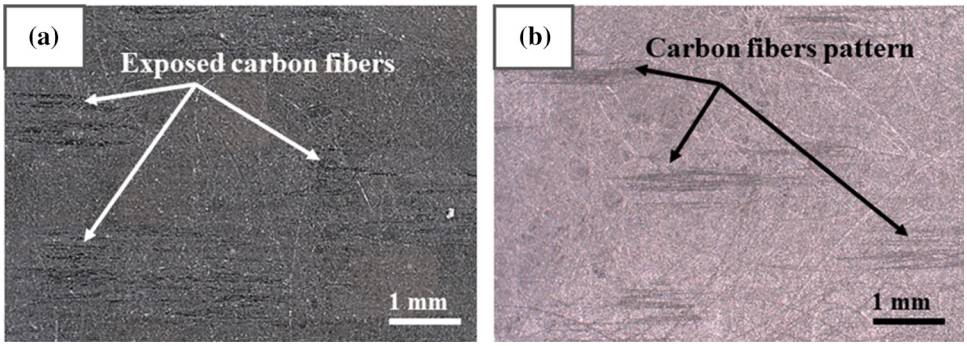

Fig. 4 Keyence digital microscope images of the (a) CFRP substrate and (b) backing surface of the EN coating after performing the adhesion strength test

Effect of CFRP Surface Characteristics on EN Coating Formation Mechanisms

In the EN coating deposition of non-conductive surfaces (i.e., epoxy regions which constituted the majority of the CFRP surface), the first step after surface cleaning is surface catalysis by reducing Pd ions to Pd atoms from a colloidal solution containing $PdCl_2$ and $SnCl_2$ (Ref 38-40). In this study, Pd particles were electrochemically activated on the heterogeneous surface features of the CFRP, containing regions of epoxy and carbon fibers. Figure 6 shows the SEM images of the CFRP surface after the Pd activation and the corresponding EDS results. As shown, Pd nanoparticles (bright spots) with an average particle size of 45 ± 5 nm were distributed over the entire surface of CFRP, but with greater accumulation on exposed carbon fiber areas. The volume fraction of Pd particles was measured to be 15%. Catalytically active Pd nanoparticles act as nucleation seeds to initiate subsequent autocatalytic (self-reduction) chemical reactions occurring during electroless deposition. The catalysis, activation and electroless deposition processes have been described previously (Ref 27).

Figure 6(a) and (b) shows the SEM images of the CFRP surface for two distinct regions of epoxy and carbon fibers, respectively. As shown, fewer Pd nanoparticles (indicated by the red arrows) are dispersed in the epoxy region as compared to the area with exposed carbon fibers. According to Fig. 6(b), Pd particles accumulate on both carbon fibers and the epoxy areas in between these carbon fibers. The preferential dispersion of the Pd nanoparticles on the carbon fiber regions might be attributed to the physical and chemical properties of carbon fibers and the inhomogeneous surface profile of the CFRP. It has been reported in the literature that carbon materials such as graphite, activated carbon, carbon fibers and carbon nanotubes are common and suitable catalyst support materials for various chemical reactions. Carbon fibers have been found to be a promising support for the catalysis of noble metals such as Pd and Pt due to their large specific surface area, high porosity, excellent electron conductivity and chemical inertness (Ref 41). The specific surface area of carbon fibers has been reported to be high, 1000-3000 (m^2/g), which provides a high available surface area for accumulation of the active Pd metal atoms (Ref 42, 43).

The observed damage to the epoxy in between the carbon fibers and inhomogeneous distribution of Pd particles could mainly be supported by the surface profile of the CFRP. The surface profile of the epoxy-CFRP substrate was characterized over an area of 6008×6008 μm^2 to study a potential relationship between the substrate surface roughness, accumulation of Pd nanoparticles and the adhesion behavior of the EN coating. Figure 7 shows the surface profile of the CFRP substrate before Pd activation. As shown, epoxy areas (red regions) are at the same level in height; however, carbon fibers (green-yellow regions) have greater depth than the epoxy area and are separated by the epoxy polymer (red regions between green-yellow lines). The maximum height (S_z) was measured to be 13.74 μm which is the sum of the largest peak height and the largest pit depth for the given field of view. The surface topology of the CFRP substrate would suggest two distinct regions of 'smooth' epoxy area and 'rough' carbon fiber regions. In previous studies (Ref 44), surface etching of the polymeric substrates using aggressive chemicals was attempted prior to Pd activation to introduce micropores on the surface and subsequently to enhance mechanical anchoring of Pd particles to the surface.

Once the CFRP is activated by Pd particles, nucleation of Ni atoms mainly starts from the activated sites (Pd particles) followed by film growth during electroless Ni deposition (Ref 38). Nickel ions adsorb onto the catalytic CFRP surface and reduce as a result of the oxidation reaction of the reducing agent (hypophosphite anion) to form a Ni-P film (see Eq 1) (Ref 45). It is well established that as-plated EN film is a metastable binary Ni-P alloy (Ref 46), formed by:

$$Ni^{2+} + 4H_2PO_2^- + H_2O \rightarrow Ni + 3H_2PO_3^- + P + H^+ + \frac{3}{2}H_2 \quad \text{(Eq 1)}$$

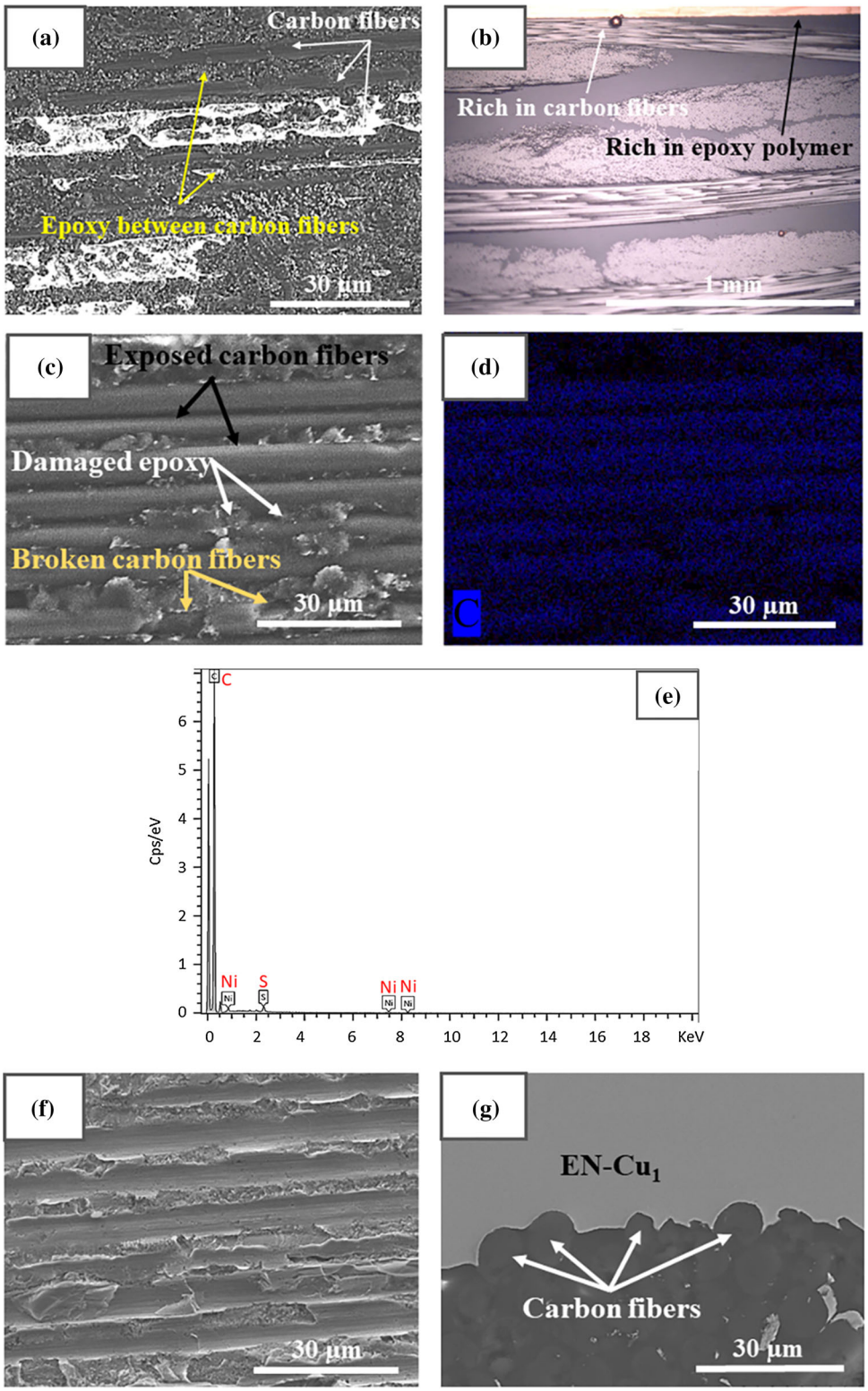

Fig. 5 (a) Top and (b) cross-section views of as-received CFRP, (c) SEM image, (d) EDS map and (e) EDS results of the CFRP surface after the adhesion strength test. SEM images of the (f) peeled EN coating and (g) polished cross section of the carbon fiber region of CFRP

Figure 8 shows the spherical nodular SEM microstructures of the EN coating after 15 s, 1 min, and 15 min of deposition. After 15 s of deposition, when there were still gaps between the particles (Fig. 8a), Ni particles with an average size of 34 ± 6 nm nucleated and grew in the vicinity of previously dispersed active Pd particles (indicated by red arrows). Nickel islands were then uniformly

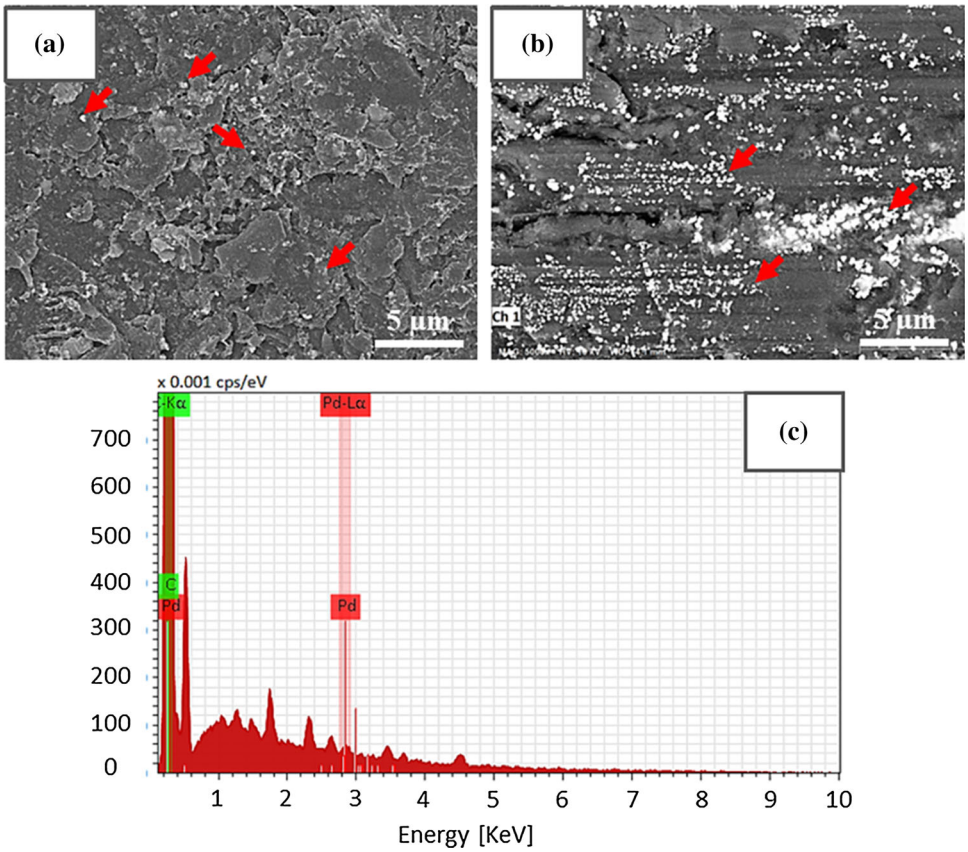

Fig. 6 SEM images of the CFRP after Pd activation in the (a) epoxy and (b) carbon fiber regions. (c) corresponding EDS data of the image (b). (Note bright spots in (a) and (b) indicate Pd particles which are shown by red arrows) (Color figure online)

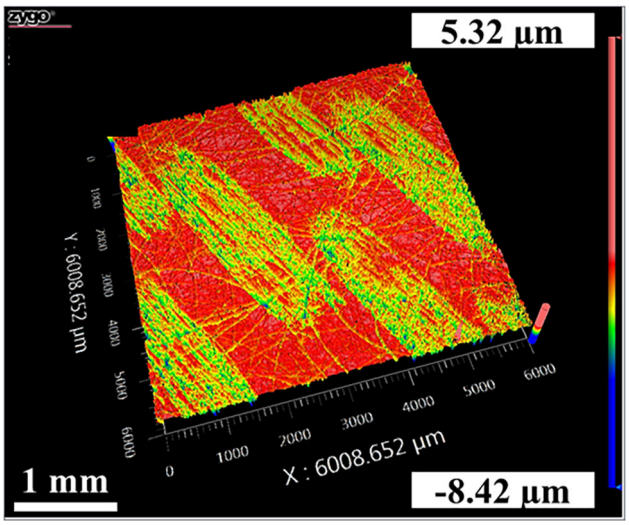

Fig. 7 Height profile of the epoxy-CFRP substrate before Pd activation

distributed and formed on the catalytic surface until the catalytic sites were covered by the Ni particles. Since Ni itself is a catalyst metal, Ni ions can be continuously reduced to Ni atoms and deposited on the previously formed layer or fill the gaps between the islands. After 1 min of self-continuing chemical reactions, the isolated islands grew by joining the subsequent Ni particles through self-catalytic effect, leading to the formation of a dense, homogeneous and uniform nodular Ni-P film on the surface (Fig. 8b). In Fig. 8(c), it can be seen that the EN coating was initially formed on the carbon fibers (shown by the white arrows), where greater Pd intensity was located. After 15 min of EN deposition, larger particles were formed through a lateral/vertical growth mechanism, leading to the formation of nodular microstructure, as has been reported previously (Ref 47).

Characterization of Fractured Surfaces in the EN-Cu_1-Cu_2 Coating Configuration

Figure 9 shows the SEM observations of the backside of the removed coatings (a, b, and c) and of the corresponding remains of the Cu coatings (d, e and f) cold sprayed at 60, 65 and 68 psi, respectively. As shown, plastically deformed Cu particles are spread out over the surface and no dimpling of the surface is observed. No significant change in the splat diameter was apparent after varying the gas pressure due to the small gas pressure range, despite the slight increase in the cohesion strength of the cold-sprayed Cu coating, rising from 1.45 to 2.95 MPa.

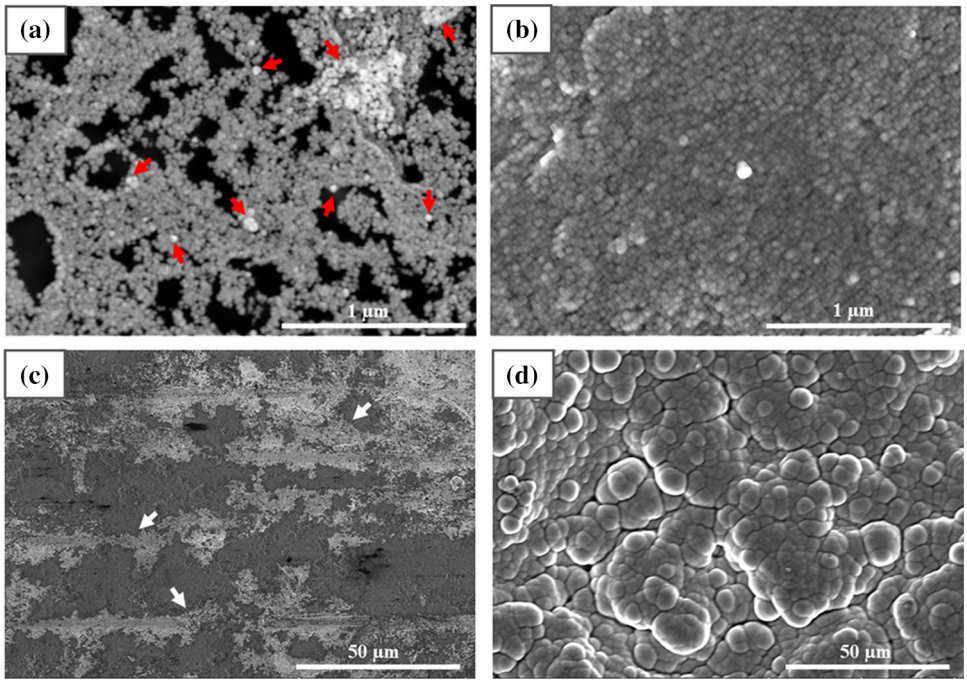

Fig. 8 High magnification SEM images of EN coating fabricated for (a) 15 s and (b) 1 min. Low magnification SEM images of the EN coating fabricated on carbon fibers after (c) 15 s and (d) 15 min. (Note the red and white arrows indicate Pd particles and EN coating in (a) and (c), respectively) (Color figure online)

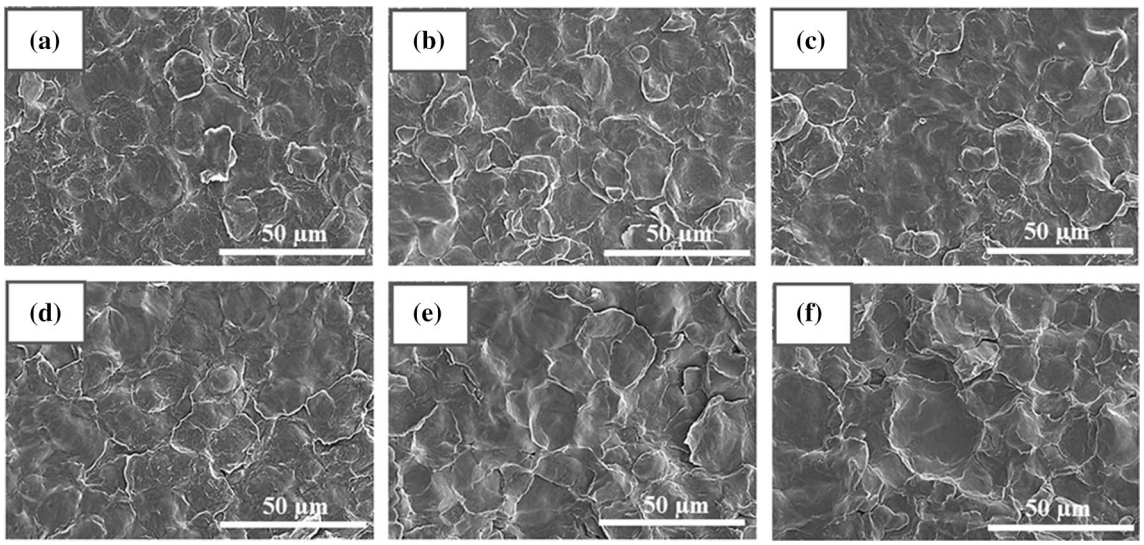

Fig. 9 (a-c) SEM images of the backside of the removed coatings and (d-f) corresponding remained Cu coatings cold sprayed at 60, 65 and 68 psi, respectively

Scratch Adhesion Bond Strength

Scratch adhesion testing was performed on cross-sections of the coatings. According to ISO/WD 27307, two types of failure can be generated as a result of scratch adhesion testing. The type of failure can be identified by observing the damage generated within/around the scratch track (Ref 48, 49). Adhesive failure occurs when cracks are initiated and propagated at the coating/substrate or coating/coating interfaces, and cone-shaped fracture occurs at the interfaces. In cohesive failure, cone-shaped fracture and crack generation take place in the coating (Ref 50).

For the scratch testing load used, there was no adhesive failure at the interfaces for all coatings. However, cone-shaped fractures and cracks occurred inside the cold-sprayed coatings, indicating the cohesive failure. Therefore, scratch testing was used to characterize cohesive failure mechanisms. Figure 10 shows the SEM and OM images of the scratch tracks obtained from the cross-sections of cold-sprayed and electroplated coatings at which

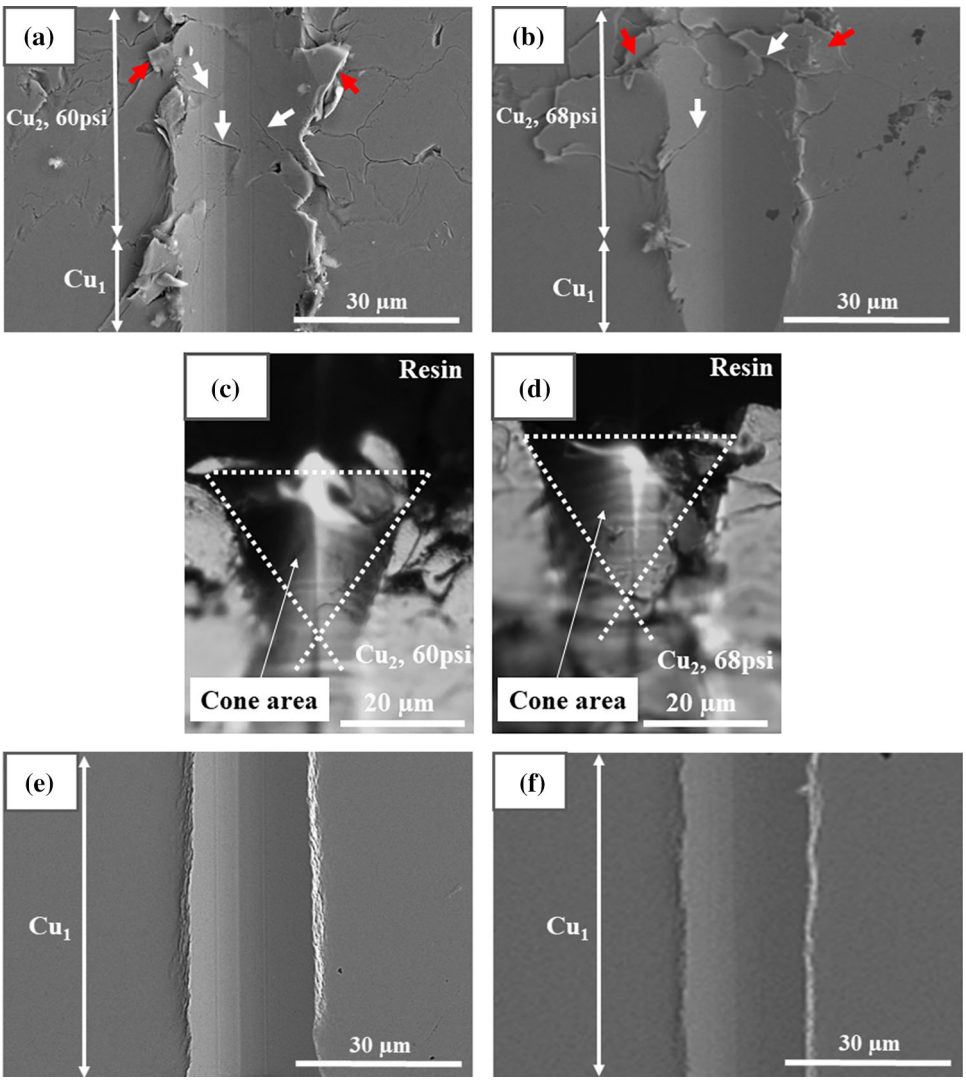

Fig. 10 (a) and (b) SEM images of the scratch tracks in the cold-sprayed coatings, (c) and (d) OM images of the cone-shaped fracture in the cold-sprayed coatings, (e) and (f) SEM images of the scratch tracks in the electroplated regions after cold spraying at 60 and 68 psi, respectively

the stylus was drawn starting from the substrate toward the cold-sprayed coating. In Fig. 10(a) and (b), the presence of cracks within the cold-sprayed coatings indicates cohesive failure (shown by the white arrows). This type of failure (through crack generation) has been reported in previous studies for ductile coatings such as Cu (Ref 48).

Figure 10(c) and (d) shows the OM images of the cone-shaped fracture occurred in the cold-sprayed coatings. Cold-sprayed coatings showed almost similar projected cone areas, suggesting almost similar cohesion bond strength by increasing the pressure from 60 to 68 psi. The similarity of the cohesive failure behavior of these cold-sprayed Cu coatings was likely due to the small gas pressure difference. In addition, Cu flakes can also be observed within both cold-sprayed Cu coatings (Fig. 10a and b), which might be an indication of particle decohesion in this region. In this case, the damage was transferred to the material adjacent (shown by red arrows) as a result of the particle decohesion.

No cracks were observed at the electroplated/cold-sprayed interface for both coatings sprayed at 60 and 68 psi gas pressures. An improved bonding at the Cu_1/Cu_2 interface is likely due to the hardness similarity of the particle to the underlying electroplated coating that allowed for mutual plastic deformation of both material couples, resulting in an enhanced mechanical/metallurgical bonding (Ref 27, 28). In this stage, the very first layer of particles adheres to the substrate and determines the adhesive strength of the coating to the substrate. In Fig. 10(e) and (f), no sign of failure was observed within the electroplated coatings, neither on the scratch track nor on the surrounding.

Microstructure Analysis

ECCI was performed on cross-sections of the feedstock Cu powder, electroplated, and cold-sprayed Cu coatings to reveal initial and deformed microstructures. Figure 11

shows the ECC images of the cross-sectioned Cu powder with low and high magnifications. As is shown, the grain structure of the Cu powder reveals an equiaxed grain microstructure with a grain size ranging from 1 to 4 μm with an average grain size of 2 ± 1 μm (Fig. 11b).

Figure 12 illustrates the ECC images of the cross-sectioned Cu coatings electroplated (Fig. 12a) and cold sprayed at pressures of 60 and 68 psi (Fig. 12c and e, respectively). Figure 12(b), (d), and (f) shows the enlarged views of the rectangles indicated in Fig. 12(a), (c), and (e),

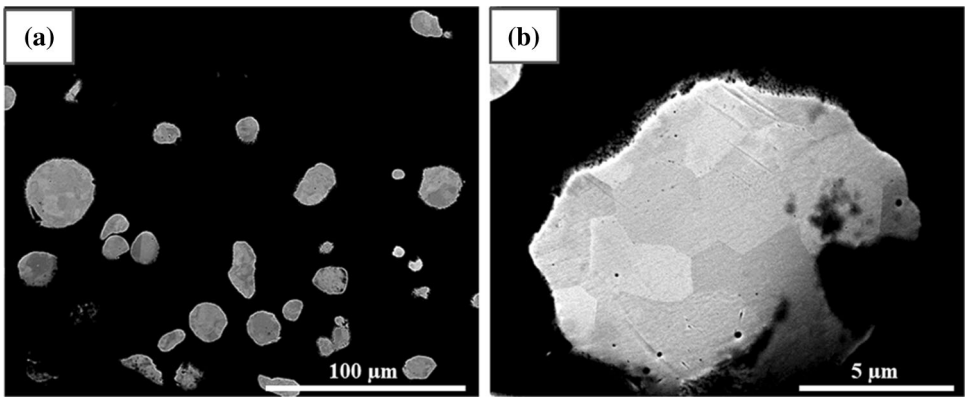

Fig. 11 ECCI micrographs of the cross-section of the feedstock Cu powder with (a) low and (b) high magnifications

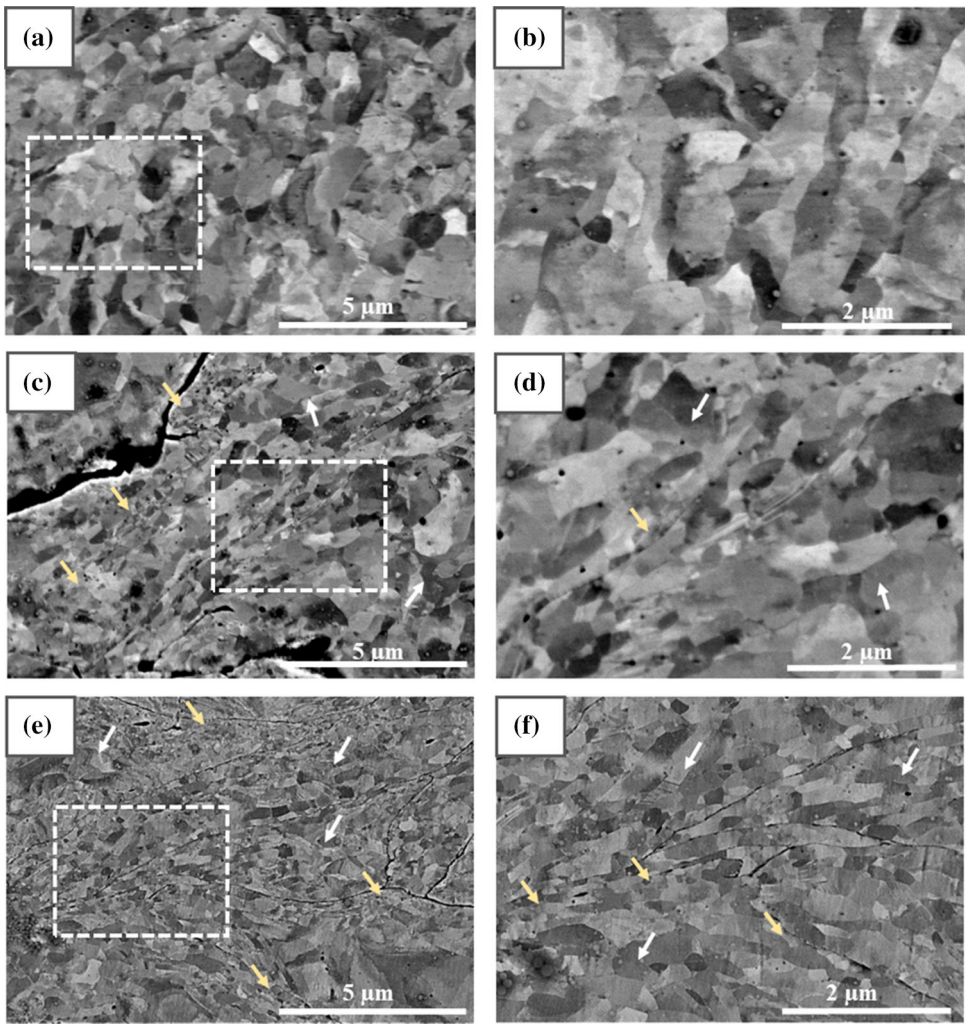

Fig. 12 ECC images of cross-sections of (a) Cu electroplated coating, (c) and (e) Cu coatings sprayed at 60 and 68 psi, respectively. (b), (d) and (f) are enlarged views of the white rectangles in (a), (c) and (e), respectively. (Note the impact direction of the Cu powder is from top to the bottom)

respectively. A more uniform microstructure was observed for the electroplated Cu coating compared to the cold-sprayed Cu coatings. For electroplated Cu coating, the average grain size was 900 ± 150 nm. However, inhomogeneous microstructures were observed for cold-sprayed Cu coatings fabricated at 60 and 68 psi gas pressures. For both cold-sprayed Cu coatings (Fig. 12c and e), the microstructure near the splat interfaces is fine grained, indicating the occurrence of dynamic recrystallization (Ref 51, 52), while a coarser structure can be observed in the central area of the particles (fine and coarse sub-structures are indicated by yellow and white arrows, respectively.) For the cold-sprayed Cu coating fabricated at 60 psi (Fig. 12c), the average grain size of the refined and coarse structures was 217 ± 75 and 700 ± 270 nm, respectively, which is significantly lower than that of feedstock Cu powder (2 ± 1 μm). By increasing the pressure from 60 to 68 psi, a decrease in the average grain size of the two sub-structures was obtained. For the cold-sprayed Cu coating fabricated at 68 psi (Fig. 12e), 530 ± 170 and 160 ± 60 nm were the average grain size of the coarse and refined structures, respectively.

It should be noted that combining ECCI and EBSD analysis may lead to a better understanding of the dynamic recrystallization and crystallographic orientation of materials which will be studied in a future work.

Discussion

Adhesion/Cohesion Bond Strengths of Multilayered Coatings

The primary influencing features observed in the fractured surfaces for the EN and EN-Cu_1 coatings were exposed carbon fibers and the associated epoxy regions. Damaged or removed epoxy in areas where exposed carbon fibers were present and locally broken carbon fibers (Fig. 5c) indicate an enhanced mechanical bonding between the EN coating and the carbon fiber areas relative to the pure epoxy region. Inhomogeneous surface topology of the CFRP (i.e., the presence of "rough" carbon fiber regions and "smooth" epoxy area) may possibly affect the overall adhesion strength of the Ni coating to CFRP. However, it is not possible to investigate the contribution of these two surface features as the tensile adhesion test is being conducted on a certain surface area that includes both epoxy and carbon fiber regions. Therefore, the measured adhesion strength is a result of contributions of both surface features.

The presence of peaks and valleys on the exposed carbon fiber regions relative to the smooth epoxy area where carbon fiber is not exposed, allowed for an enhanced anchoring of Pd nanoparticles to micropores of the carbon fiber regions and the subsequent enhanced mechanical bonding between the EN coating and these areas (Fig. 6a and b). The little-observed presence of Ni (Fig. 5c and e) on the CFRP surface after the adhesion test indicated that the bonding between EN coating and CFRP is mostly adhesive. These results suggest that the adhesion by mechanical anchoring between the EN coating and the CFRP could be enhanced by increasing the areal fraction of exposed carbon fibers.

After cold spray deposition of Cu at 60-68 psi, weak cohesion strengths were obtained in the Cu_2 part of the EN-Cu_1-Cu_2 coating configuration (Fig. 3). Fractured surfaces (Fig. 9) showed no dimpling of the surface, indicating a lack of metallurgical bonding between the deformed particles, thus leading to cohesive failure within cold-sprayed coatings for all gas pressures. It was previously reported that the velocity of Cu particles sprayed at 60-68 psi was close to the critical velocity of Cu (on the order of 500 m/s) (Ref 28, 53). Weak inter-particle bonding is likely attributed to the low kinetic energy of the particles sprayed close to this velocity. However, applying higher gas pressure than 68 psi and temperatures higher than 482 °C was not possible in this study due to the observed coating delamination (Ref 27). Delamination was hypothesized to be due to the insufficient coating adhesion to the CFRP substrate and thermal stress being introduced to the coating because of the difference in thermal expansion coefficient. There are several ways to increase the adhesion bond strength of the coating to the polymeric substrates such as chemical, mechanical and plasma treatments of the substrate before the metallization step (Ref 54). It would be expected that microscopic voids, peaks and valleys would be generated on the surface, promoting the mechanical anchoring between the metallic coating and the polymeric substrate. Another method to tackle delamination would be to increase the interlayer thickness to enhance energy absorption and facilitate heat dissipation.

From scratch adhesion testing, it was found that for the given scratch condition, the obtained results correlate with those obtained from the tensile adhesion testing (Fig. 10). Note that both tensile and scratch testing conditions may affect the failure mechanism behavior of the coatings. In a previous study (Ref 55), a direct correlation between the results obtained from scratch and tensile adhesion testing was not obtained and the type of failure for the same coating was different when both methods were employed. However, scratch testing is a practical, efficient and quick method to identify the type of bond strength (adhesive/cohesive) that can be used as a supplement to ASTM Standard C-633-13 adhesion testing.

Coating Microstructure

As observed in the ECC images of the coatings (Fig. 12), the non-uniform microstructure within cold-sprayed coatings is associated with an inhomogeneous plastic deformation of the cold-sprayed Cu particles. In cold spray, particle interfacial regions experience more severe plastic deformation, strain rate and associated temperature rise, resulting in recrystallization and an inhomogeneous coating microstructure (Ref 52, 56). In a recent study (Ref 28), the temperature profile of the Cu particle impacted onto a Cu interlayer at a gas pressure of 65 psi was analyzed and reported using finite element simulation. The temperature profile of the impacted Cu particle revealed an increase in temperature from 200 °C (central region of the particle) to 700 °C (particle interfacial region), leading to an inhomogeneous degree of recrystallization within the particle.

A decrease in the grain size of the cold-sprayed coating by increasing the pressure is attributed to the higher degree of plastic deformation and increase in dislocation density. Similar microstructural features have been reported for cold-sprayed coatings (Ref 51, 52, 57). In a previous study (Ref 27), the microhardness of the feedstock Cu powder, electroplated and cold-sprayed Cu coatings was measured and reported. The copper powder had a microhardness of 65 $\pm$ 5 HV, which was lower than that of cold-sprayed Cu coatings. The average microhardness of the cold-sprayed Cu coatings fabricated at pressures of 60 and 68 psi was found to be 100 $\pm$ 5 and 118 $\pm$ 5 HV, respectively. An increased microhardness of the cold-sprayed Cu coatings relative to the Cu powder is related to the extensive plastic deformation, increased dislocation density and grain refinement (Ref 58). An increased microhardness of the coating cold sprayed at 68 psi compared to that of 60 psi is due to the more severe plastic deformation and consequently smaller average grain size of both sub-structures. It can also be found that the smaller average grain size of the cold-sprayed coatings as compared to the electroplated Cu coating led to an increase in the hardness of the cold-sprayed coating relative to the electroplated coating (75 HV versus 100 and 118 HV).

Conclusions

The adhesion/cohesion bond strength of multilayered metallic coatings fabricated onto CFRP substrate was studied through tensile and scratch adhesion testing, and fracture surfaces characterization. The results indicated that failure was almost adhesive at the EN/CFRP interface in the EN and EN-Cu_1 coatings. Damaged epoxy and broken carbon fibers indicated enhanced mechanical anchoring between the EN coating and carbon fiber regions. This enhanced bonding was possibly due to the increased roughness leading to the large accumulation and anchoring of Pd nanoparticles in these areas. From the scratch adhesion testing of the EN-Cu_1-Cu_2 coating, cone-shaped fractures and cracks were observed within cold-sprayed Cu coatings, indicating cohesive failure. Failure of the cold-sprayed Cu coatings was likely due to the poor inter-particle bonding, absence of dimpling and limited plastic deformation of the particles at low gas pressures. A direct correlation between the tensile and scratch adhesion testing was obtained.

Microstructural analysis of the cold-sprayed Cu coatings through ECC imaging revealed inhomogeneous microstructure with grain refinement at the splat boundaries due to the higher degree of plastic deformation. However, a more uniform microstructure was achieved for the electroplated Cu coating with a larger average grain size as compared to that of cold-sprayed Cu coatings. The lower hardness of the electroplated Cu coating compared to the cold-sprayed Cu coatings was attributed to the larger average grain size and different microstructural characteristics.

Acknowledgments The authors would like to acknowledge the financial support of the Natural Sciences and Engineering Research Council of Canada (NSERC) through the Green Surface Engineering for Advanced Manufacturing (Green SEAM) Strategic Network [grant number NETGP 493955-16]. In addition, the industrial partner, Bombardier Aerospace, is gratefully acknowledged. We wish to thank the National Research Council Canada and Mr. Kevin Bricault for their assistance with the cold spray experiments. Dr. Lise Guichaoua from the McGill Materials Services Electron Microscopy Labs is gratefully acknowledged for her help with the SU8230.

References

1. U.S. Department of Transportation Federal Aviation Administration, Aviation Maintenance Technician Handbook—Airframe Vol. 1 (2012)
2. J. Siegel and V. Kotál, Preparation of Thin Metal Layers on Polymers, *Acta Polytech.*, 2007 https://doi.org/10.14311/904
3. T. Duguet, F. Senocq, L. Laffont and C. Vahlas, Metallization of Polymer Composites by Metalorganic Chemical Vapor Deposition of Cu: Surface Functionalization Driven Films Characteristics, *Surf. Coat. Technol.*, 2013, **230**, p 254-259.
4. S. Kuroda, J. Kawakita, M. Watanabe and H. Katanoda, Warm Spraying—A Novel Coating Process Based on High-Velocity Impact of Solid Particles, *Sci. Technol. Adv. Mater.*, 2008, **9**(3), p 17.
5. C. Katsoulis, B.K. Kandola, P. Myler and E. Kandare, Post-Fire Flexural Performance of Epoxy-Nanocomposite Matrix Glass Fibre Composites Containing Conventional Flame Retardants, *Compos. Part A Appl. Sci.*, 2012, **43**(8), p 1389-1399.
6. J. Affi, H. Okazaki, M. Yamada and M. Fukumoto, Fabrication of Aluminum Coating onto CFRP Substrate by Cold Spray, *Mater. Trans.*, 2011, **52**(1), p 1759-1763.
7. N. Huonnic, M. Abdelghani, P. Mertiny and A. McDonald, Deposition and Characterization of Flame-Sprayed Aluminum on

Cured Glass and Basalt Fiber-Reinforced Epoxy Tubes, *Surf. Coat. Technol.*, 2010, **205**(3), p 867-873.
8. R. Gonzalez, H. Ashrafizadeh, A. Lopera, P. Mertiny and A. McDonald, A Review of Thermal Spray Metallization of Polymer-Based Structures, *J. Therm. Spray Technol.*, 2016, **25**(5), p 897-919.
9. S. Kuroda, J. Kawakita, M. Watanabe, K.H. Kim, R. Molak and H. Katanoda, Current Status and Future Prospects of Warm Spray Technology, *Future Development of Thermal Spray Coatings*. Woodhead Publishing, 2015, p 163-206. https://doi.org/10.1016/B978-0-85709-769-9.00007-5
10. C. Chen, X. Xie, Y. Xie, X. Yan, G. Huang, S. Deng, Z. Ren and H. Liao, Metallization of Polyether Ether Ketone (PEEK) by Copper Coating via Cold Spray, *Surf. Coat. Technol.*, 2018, **342**, p 209-219.
11. A. Papyrin, V. Kosarev, S. Klinkov, A. Alkhimov and V.M. Fomin, *Cold Spray Technology*, Elsevier, 2007.
12. V.K. Champagne, *The Cold Spray Materials Deposition Process: Fundamentals and Applications*, Elsevier, 2007.
13. H. Che, P. Vo and S. Yue, Metallization of carbon Fibre Reinforced Polymers by Cold Spray, *Surf. Coat. Technol.*, 2017, **313**, p 236-247.
14. A. Ganesan, M. Yamada and M. Fukumoto, Cold spray Coating Deposition Mechanism on the Thermoplastic and Thermosetting Polymer Substrates, *J. Therm. Spray Technol.*, 2013, **22**(8), p 1275-1282.
15. H. Che, P. Vo and S. Yue, Metallization of various polymers by cold spray, *J. Therm. Spray Technol.*, 2017, **27**(1-2), p 169-178.
16. P. Lomonaco, S. Weiller, I. Feki, A. Debray, F. Delloro, M. Jeandin, B. Favini and C. Rossignol, Cold Spray Technology to Promote Conductivity of Short Carbon Fiber Reinforced Polyether-Ether-Ketone (PEEK), *Key Eng. Mater.*, 2019, **813**, p 459-464.
17. V. Gillet, E. Aubignat, S. Costil, B. Courant, C. Langlade, P. Casari, W. Knapp and M.P. Planche, Development of Low Pressure Cold Sprayed Copper Coatings on Carbon Fiber Reinforced Polymer (CFRP), *Surf. Coat. Technol.*, 2019, **364**, p 306-316.
18. R. Della Gatta, A. Viscusi, A.S. Perna, A. Caraviello and A. Astarita, Feasibility of Steel Powder Deposition on Composites Through Cold Spray, *Mater. Manuf. Process.*, 2020, **36**(3), p 281-291.
19. M. Barletta, A. Gisario and V. Tagliaferri, Electrostatic Spray Deposition (ESD) of Polymeric Powders on Thermoplastic (PA66) Substrate, *Surf. Coat. Technol.*, 2006, **201**(1-2), p 296-308.
20. G. Archambault, B. Jodoin, S. Gaydos and M. Yandouzi, Metallization of Carbon Fiber Reinforced Polymer Composite by Cold Spray and Lay-up Molding Processes, *Surf. Coat. Technol.*, 2016, **300**, p 78-86.
21. A. Ganesan, J. Affi, M. Yamada and M. Fukumoto, Bonding Behavior Studies of Cold Sprayed Copper Coating on the PVC Polymer Substrate, *Surf. Coat. Technol.*, 2012, **207**, p 262-269.
22. M. Chen, Surface preparation of polymeric substrates for cold spraying coatings, Masters thesis, McGill University (2022)
23. A. Liberati, Mechanisms affecting the metallization of carbon fiber reinforced polymers through the cold spraying of Sn-based mixed metal powders, Ph.D. thesis, McGill University (2022)
24. A.C. Liberati, H. Che, P. Fallah, P. Vo and S. Yue, Pull-off Testing and Electrical Conductivity of Sn-Based Metal Powder Mixtures Cold Sprayed on Carbon Fiber-Reinforced Polymers, *J. Therm. Spray Technol.*, 2022 https://doi.org/10.1007/s11666-022-01405-0
25. A. Małachowska, M. Winnicki, Ł Konat, T. Piwowarczyk, L. Pawłowski, A. Ambroziak and M. Stachowicz, Possibility of Spraying of Copper Coatings on Polyamide 6 with Low Pressure Cold Spray Method, *Surf. Coat. Technol.*, 2017, **318**, p 82-89.
26. A. Rezzoug, S. Abdi, A. Kaci and M. Yandouzi, Thermal Spray Metallisation of Carbon Fibre Reinforced Polymer Composites: Effect of Top Surface Modification on Coating Adhesion and Mechanical Properties, *Surf. Coat. Technol.*, 2018, **333**, p 13-23.
27. P. Fallah, S. Rajagopalan, A. McDonald and S. Yue, Development of Hybrid Metallic Coatings on Carbon Fiber-Reinforced Polymers (CFRPs) by Cold Spray Deposition of Copper-Assisted Copper Electroplating Process, *Surf. Coat. Technol.*, 2020, **400**, p 126231.
28. P. Fallah, R. Chakrabarty, J. Song, A. McDonald and S. Yue, Effect of Metallic Interlayer Hardness on Deposition Characteristics of Cold-Sprayed Copper Particles on Carbon Fiber-Reinforced Polymers, *J. Therm. Spray Technol.*, 2022, **31**(3), p 559-573.
29. ASTM, ASTM C 633—Standard Test Method for Adhesion or Cohesion Strength of Thermal Spray Coatings. Annual Book of ASTM Standards (2008)
30. International A, ASTM C633-13, Standard Test Method for Adhesion or Cohesion Strength of Thermal Spray Coatings. 2017: West Conshohocken, PA
31. ISO-ISO 27307:2015, Thermal spraying—Evaluation of adhesion/cohesion of thermal sprayed ceramic coatings by transverse scratch testing
32. M. Cailler and G.H. Lee, Scratch Adhesion Test of Magnetron-Sputtered Copper Coatings on Aluminium Substrates: Effects of the Surface Preparation, *Thin Solid Films*, 1989, **168**(2), p 193-205.
33. M. Schlesinger and M. Paunovic, *Modern Electroplating*, 5th ed. John Wiley & Sons, 2014.
34. G.O. Mallory and J.B. Hajdu, *Electroless Plating: Fundamentals and Applications*, William Andrew, 1990.
35. P. Bindra, Mechanisms of Electroless Metal Plating, *J. Electrochem. Soc.*, 1983, **130**(11), p 1112.
36. S.J. Yu, L.X. Song, Y.S. Huang, R.G. Zhao, X.F. Hu, Electroless Ni-P-SiC Composite Coating. Inorg. Mater. **19**(3) (2004)
37. J.N. Balaraju, P. Radhakrishnan, V. Ezhilselvi, A.A. Kumar, Z. Chen and K.P. Surendran, Studies on Electroless Nickel Polyalloy Coatings Over Carbon Fibers/CFRP Composites, *Surf. Coat. Technol.*, 2016, **302**, p 389-397.
38. R. Agarwala, V. Agarwala and R. Sharma, Electroless Ni-P Based Nanocoating Technology—A Review, Synthesis and Reactivity in Inorganic, *Inorg. Nano Met. Chem.*, 2006, **36**(6), p 493-515.
39. J.N. Balaraju and K.S. Rajam, Electroless Deposition of Ni-Cu-P, Ni-W-P and Ni-W-Cu-P Alloys, *Surf. Coat. Technol.*, 2005, **195**(2-3), p 154-161.
40. K. Yamagishi, N. Okamoto, N. Mitsumata, N. Fukumuro, S. Yae and H. Matsuda, Reaction process of two-step Catalysation Pretreatment for Electroless Plating on Non-conducting Substrates, *Trans. Inst. Met. Finish.*, 2004, **82**(3-4), p 114-117.
41. H. Jüntgen, Activated Carbon as Catalyst Support: A Review of New Research Results, *Fuel*, 1986, **65**(10), p 1436-1446.
42. E. Lam and J.H.T. Luong, Carbon Materials as Catalyst Supports and Catalysts in the Transformation of Biomass to Fuels and Chemicals, *ACS Catal.*, 2014, **4**(10), p 3393-3410.
43. M. Luty-Błocho, M. Wojnicki, K. Pacławski and K. Fitzner, The Synthesis of Platinum Nanoparticles and their Deposition on the Active Carbon Fibers in One Microreactor Cycle, *Chem. Eng. J.*, 2013, **226**, p 46-51.
44. M. Charbonnier and M. Romand, Polymer Pretreatments for Enhanced Adhesion of Metals Deposited by the Electroless Process, *Int. J. Adhes. Adhes.*, 2003, **23**(4), p 277-285.
45. C.K. Lee, Structure, Electrochemical and Wear-Corrosion Properties of Electroless Nickel-Phosphorus Deposition on CFRP Composites, *Mater. Chem. Phys.*, 2009, **114**(1), p 125-133.

46. J.E. Van Den Meerakker, On the Mechanism of Electroless Plating. II. One Mechanism for Different Reductants, *J. Appl. Electrochem.*, 1981, **11**(3), p 395-400.
47. S. Wei, X. Zhan, Y. Wen, Y. Li, Z. Zhang, F. Wu and C. Wang, Deposition Mechanism of Electroless Nickel Plating of Composite Coatings on Magnesium Alloy, *Chem. Eng. Sci.*, 2019, **207**, p 1299-1308.
48. S.J. Bull, Failure Modes in Scratch Adhesion Testing, *Surf. Coat. Technol.*, 1991, **50**(1), p 25-32.
49. R.F. Váz et al., Fretting Wear and Scratch Resistance of Cold-Sprayed Pure Cu and Ti, *Metallogr. Microstruct. Anal.*, 2021, **10**(4), p 496-513.
50. V. Aleksandar, S. Arostegui, G. Favaro, F. Zivic, M. Mrdak, S. Mitrović and V. Popovic, Evaluation of Adhesion/Cohesion Bond Strength of the Thick Plasma Spray Coatings by Scratch Testing on Coatings Cross-Sections, *Tribol. Int.*, 2011, **44**(11), p 1281-1288.
51. T. Liu, J.D. Leazer and L.N. Brewer, Particle Deformation and Microstructure Evolution During Cold Spray of Individual Al-Cu Alloy Powder Particles, *Acta Mater.*, 2019, **168**, p 13-23.
52. M.R. Rokni, S.R. Nutt, C.A. Widener, V.K. Champagne and R.H. Hrabe, Review of Relationship Between Particle Deformation, Coating Microstructure, and Properties in High-Pressure Cold Spray, *J. Therm. Spray Technol.*, 2017, **26**, p 1308-1355.
53. T. Schmidt, F. Gärtner, H. Assadi and H. Kreye, Development of a Generalized Parameter Window for Cold Spray Deposition, *Acta Mater.*, 2006, **54**(3), p 729-742.
54. M. Hamdi, M.N. Saleh and J.A. Poulis, Improving the Adhesion Strength of Polymers: Effect of Surface Treatments, *J. Adhes. Sci. Technol.*, 2020, **34**(17), p 1853-1870.
55. A. Vencl et al., Evaluation of Adhesion/Cohesion Bond Strength of the Thick Plasma Spray Coatings by Scratch Testing on Coatings Cross-Sections, *Tribol. Int.*, 2011, **44**(11), p 1281-1288.
56. C. Borchers, R. Gärtner, T. Stoltenhoff and H. Kreye, Microstructural Bonding Features of Cold Sprayed Face Centered Cubic Metals, *J. Appl. Phys.*, 2004, **96**(8), p 4288.
57. V.N.V. Munagala, V. Akinyi, P. Vo and R.R. Chromik, Influence of Powder Morphology and Microstructure on the Cold Spray and Mechanical Properties of Ti6Al4V Coatings, *J. Therm. Spray Technol.*, 2018, **27**(5), p 827-842.
58. Y. Zou, D. Goldbaum, J.A. Szpunar and S. Yue, Microstructure and Nanohardness of Cold-Sprayed Coatings: Electron Backscattered Diffraction and Nanoindentation Studies, *Scr. Mater.*, 2010, **62**(6), p 395-398.

Publisher's Note Springer Nature remains neutral with regard to jurisdictional claims in published maps and institutional affiliations.